



**Spectroelectrochemical investigations of nickel cyclam  
indicate different reaction mechanisms for electrocatalytic  
CO<sub>2</sub> and H<sup>+</sup> reduction**

Journal:	<i>Dalton Transactions</i>
Manuscript ID	DT-ART-07-2018-002873.R1
Article Type:	Paper
Date Submitted by the Author:	24-Sep-2018
Complete List of Authors:	Behnke, Shelby; The Ohio State University, Department of Chemistry and Biochemistry Manesis, Anastasia; The Ohio State University, Ohio State Biochemistry Program Shafaat, Hannah; The Ohio State University, Department of Chemistry and Biochemistry



Journal Name

ARTICLE

## Spectroelectrochemical investigations of nickel cyclam indicate different reaction mechanisms for electrocatalytic CO<sub>2</sub> and H<sup>+</sup> reduction

Shelby L. Behnke,<sup>a</sup> Anastasia C. Manesis<sup>b</sup> and Hannah S. Shafaat<sup>a,b</sup>Received 00th January 20xx,  
Accepted 00th January 20xxDOI: 10.1039/x0xx00000x  
www.rsc.org/

Rising levels of atmospheric carbon dioxide continue to motivate the development of catalysts that can efficiently convert CO<sub>2</sub> to useful products in water without substantial amounts of H<sub>2</sub> formed as a byproduct. In addition to synthetic efforts, mechanistic investigations on existing catalysts are necessary to understand the molecular factors contributing to activity and selectivity, which can guide rational improvements and increase catalyst robustness. [Ni(cyclam)]<sup>2+</sup> (cyclam = 1,4,8,11-tetraazacyclotetradecane) is one such catalyst, known for decades to be capable of selective CO<sub>2</sub> reduction to CO in water, but with little mechanistic information experimentally established or catalytic intermediates characterized. To better understand the mechanisms of aqueous H<sup>+</sup> and CO<sub>2</sub> reduction by [Ni(cyclam)]<sup>2+</sup>, spectroelectrochemical investigations were performed in conjunction with activity assays. Both large surface area glassy carbon and amorphous graphite rod working electrodes were tested, with the latter found to be significantly more active and selective for CO production. Optical, resonance Raman, and EPR spectroelectrochemical experiments on [Ni(cyclam)]<sup>2+</sup> during catalysis under N<sub>2</sub>, CO<sub>2</sub>, and CO gases show the appearance of a single species, independent of electrode used. Identical signals are observed at anodic potentials. Spectroscopic and electrochemical analysis coupled with density functional theory calculations suggest that the signals observed originate from [Ni(cyclam)(H<sub>2</sub>PO<sub>4</sub>)]<sup>2+</sup>. The generation of a Ni<sup>III</sup> species under catalytic, reducing conditions suggests an ECCE mechanism for H<sup>+</sup> reduction by [Ni(cyclam)]<sup>2+</sup>, which differs from the proton-coupled, ECEC pathway proposed for CO<sub>2</sub> reduction. The divergent mechanisms seen for the two reactions may underlie the differential reactivity of [Ni(cyclam)]<sup>2+</sup> towards each substrate, with implications for the design of increasingly selective molecular catalysts. This observation also highlights the substantial impact of buffer and electrode choice when characterizing and benchmarking the catalytic properties of new compounds.

### Introduction

Rising levels of CO<sub>2</sub> in the atmosphere have driven increasing interest in the development of catalysts that can convert this potent greenhouse gas into useful fuels via sustainable methods.<sup>1</sup> Though sometimes synthetically challenging, small-molecule catalysts are particularly useful to gain information on reaction mechanisms.<sup>2–5</sup> This information is important for the rational development of increasingly active systems. Selectivity is a particular concern for CO<sub>2</sub> reduction in water, as H<sub>2</sub> generation is thermodynamically favoured over CO production by ~110 mV.<sup>6,7</sup> The factors that dictate both selectivity and activity are important to identify in order to understand the mechanisms of catalysis for both H<sup>+</sup> and CO<sub>2</sub> reduction.

One catalyst known to selectively reduce CO<sub>2</sub> to CO with high efficiencies and turnover rates is [Ni(1,4,8,11-tetraazacyclotetradecane)]<sup>2+</sup> ([Ni(cyclam)]<sup>2+</sup>, **[1]**).<sup>8</sup> CO<sub>2</sub> can be reduced by [Ni(cyclam)]<sup>2+</sup> either photochemically or electrochemically, though the method of reduction impacts the selectivity and overall activity.<sup>9–14</sup> Previous work has shown that incorporating small-molecule catalysts such as **[1]** into stable

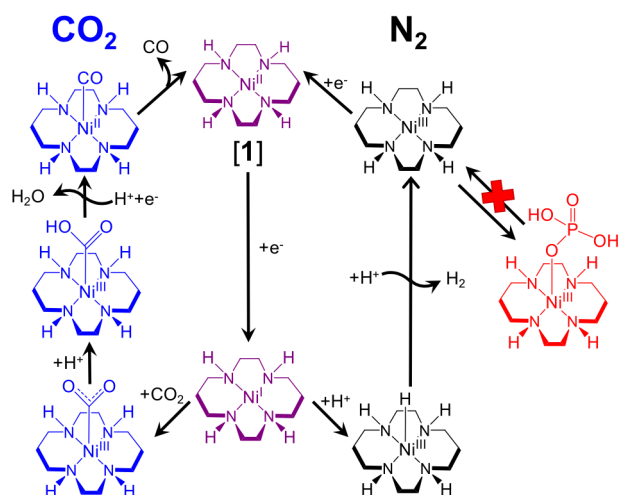
protein structures can increase both selectivity and activity.<sup>12,15–18</sup> This has been attributed to synergistic effects of the secondary and tertiary coordination spheres provided by the protein scaffold and intramolecular electron transfer, though the molecular origins of this enhancement remain experimentally unresolved.<sup>16</sup> To identify these different contributing factors, it is critical to first arrive at an understanding of the catalytic mechanism of **[1]** in solution and characterize intermediate species that are relevant to the catalytic pathway.

However, this has proven to be more challenging than previously thought. To this point, reduced Ni<sup>I</sup> and substrate-bound intermediate states have not been trapped in aqueous solution despite over 30 years of study. This is due in part to rapid poisoning of the metal catalyst by the product.<sup>19,20</sup> Instead, computational studies in conjunction with observations made from electrochemical measurements have dominated the mechanistic investigations on **[1]**.<sup>21</sup> The current hypothesis suggests that the resting state of [Ni(cyclam)]<sup>2+</sup> is first reduced to generate the active species (**Scheme 1**).<sup>9,21–23</sup> The Ni<sup>I</sup> state can then react with either a proton or carbon dioxide, depending on which substrate is present. Reversible binding of CO<sub>2</sub> to the Ni<sup>I</sup> center is thought to occur via the carbon atom.<sup>21,22</sup> The protonation of the bound CO<sub>2</sub> yields [Ni(cyclam)(COOH)]<sup>2+</sup>, followed by the rapid addition of a second proton and C–O bond cleavage to yield the product state, [Ni(cyclam)(CO)]<sup>2+</sup>, and water. Release of CO regenerates the catalyst resting state.<sup>21</sup> This proposal suggests that the mechanism proceeds through an ECEC mechanism (electron transfer - chemical step - electron transfer - chemical step),

<sup>a</sup> Department of Chemistry and Biochemistry, The Ohio State University, 100 W 18th Ave, Newman & Wolfram Laboratory of Chemistry, Columbus, OH 43210

<sup>b</sup> Ohio State Biochemistry Program, The Ohio State University, 100 W 18th Ave, Newman & Wolfram Laboratory of Chemistry, Columbus, OH 43210

Electronic Supplementary Information (ESI) available: Control experiments, raw spectroelectrochemical data, tabulated activity values, cyclic voltammograms, supplemental computational models and data. See DOI: 10.1039/x0xx00000x



**Scheme 1.** Proposed mechanisms for CO<sub>2</sub> reduction and H<sub>2</sub> production by [1].

though the intermediate steps are suggested to be concerted.<sup>22</sup> Another proposed mechanism for CO<sub>2</sub> reduction proceeds via hydride transfer, though this might be expected to yield formate rather than CO.<sup>24–26</sup>

The research to date in this field has largely focused on electrocatalysis with mercury pool electrodes due to the inherent inertness of mercury, wide potential window, and ability to amalgamate with metallic nanoparticle degradation products.<sup>27</sup> Recent work has begun including electrocatalysis at carbon-based electrodes due to issues with the toxicity and limited scalability of mercury electrodes.<sup>10,22</sup> However, different levels of activity and selectivity are seen across the two electrode materials. To further develop the utility of these environmentally friendly and inexpensive electrode materials and elucidate the distinctions underpinning this differential catalytic behavior, spectroelectrochemical studies have been performed. Both glassy carbon (GC) and amorphous graphite rod (AG) working electrodes have been used, as differences have been reported for electrocatalytic CO<sub>2</sub> and H<sup>+</sup> reduction between GC and pyrolytic graphite electrodes (PGE) in other systems.<sup>28,29</sup>

Prior studies have focused on identifying the mechanism of CO<sub>2</sub> binding and conversion by [1].<sup>21,22,30</sup> However, proton reduction remains a competing pathway, one that, if eradicated, would provide a completely selective catalyst. To identify whether H<sub>2</sub> and CO generation by [1] follow the same basic mechanistic pathway, spectroscopic studies in the presence and absence of CO<sub>2</sub> must be conducted. In this work, we report spectroelectrochemical studies on [1] using optical, resonance Raman, and electron paramagnetic resonance techniques under catalytic conditions for both H<sup>+</sup> and CO<sub>2</sub> reduction to characterize key catalytic intermediates. In conjunction with density functional theory (DFT) calculations, these results show that a [Ni(cyclam)]<sup>3+</sup> species is generated under all conditions, suggestive of an ECCE mechanism for H<sup>+</sup> reduction. The divergent catalytic schemes and proposed intermediates for CO<sub>2</sub> and H<sup>+</sup> reduction shed insight into the differential selectivity seen across organic solvents and as a function of pH. Ultimately, these observations can guide design of catalysts that

suppress H<sup>+</sup> reduction as well as provide a better understanding of the selectivity observed in [1]-bound protein systems.<sup>12,15</sup>

## Experimental

All materials were used as received unless otherwise noted. Samples were prepared with standard air-free techniques on a Schlenk line or in an anaerobic glovebox (<10 ppm O<sub>2</sub>, Vigor Technologies). All buffers were prepared using deionized water (18.2 MOhm, Elga Technologies). NiCl<sub>2</sub>·6H<sub>2</sub>O was purchased from Alfa Aesar. 1,4,8,11-tetraazacyclotetradecane (cyclam) was purchased from Acros Organics. Diethyl ether and ethanol were purchased from Fisher Scientific. The [Ni(cyclam)]<sup>2+</sup> complex ([1]) was synthesized following prior literature reports.<sup>10,31</sup> [Ni(cyclam)]SO<sub>4</sub> ([2]) was synthesized using the same procedure as [1], using a NiSO<sub>4</sub>(H<sub>2</sub>O)<sub>6</sub> precursor instead of NiCl<sub>2</sub>·6H<sub>2</sub>O. All data analysis was performed using IgorPro 7.0 (Wavemetrics, Lake Oswego, OR). All buffers were prepared such that the final, experimental pH values were 7.0.

**Warning:** The generation of a highly toxic byproduct, Ni(CO)<sub>4</sub>, can be formed during the reduction of nickel complexes in the presence of CO.

**Electrochemistry.** All electrolysis experiments were performed on a WaveNow potentiostat (Pine Instruments, Durham, NC) or a CH Instruments Model 700E Series Bipotentiostat with a graphite rod working electrode (Sigma Aldrich, St. Louis, MO), platinum wire counter electrode, and a Ag/AgCl reference electrode (Pine Instruments, Durham, NC). The Ag/AgCl reference electrode potential was converted to NHE by addition of +0.198 V to the measured potentials. All cyclic voltammetry and electrolysis experiments were performed with a large surface area glassy carbon working electrode (Type 2, Alfa Aesar, Ward Hill, MA) or an amorphous graphite rod working electrode (Sigma Aldrich, St. Louis, MO), platinum wire counter electrode, and a Ag/AgCl reference electrode. Electrolysis experiments for GC and EPR analysis were either carried out in a gas-tight scintillation vial (Thermo Scientific) with the electrodes threaded through the septum cap or inside of a 1 cm x 1 cm septum-capped cuvette with the electrodes threaded through the cap.

**Optical Spectroscopy.** Absorption spectroelectrochemistry was carried out using a Shimadzu UV-2600 Spectrometer with a 1 cm x 1 cm screw cap quartz cuvette (Starna Cells, Atascadero, CA) equipped with a gas-tight septum and a miniature stir bar. The electrodes used were pierced through the septum cap and immersed in solution. A miniature cuvette stir plate (Cimarec i, Mini Stirrer, Thermo Scientific) was used inside the cuvette holder in the spectrometer. The reference cell (1 cm x 1 cm) used for all experiments contained 50 mM phosphate buffer, pH 7.0, unless otherwise stated. The molar extinction coefficient of [1] at 450 nm has been previously reported to be 30 M<sup>-1</sup> cm<sup>-1</sup>.<sup>11</sup> During the spectroelectrochemical electrolysis experiments, the spectrometer was set to collect 100 scans (900 nm – 190 nm) over the course of 150 minutes (1 scan / 1.5 min). Control experiments containing permutations of electrolyte, nickel, and ligand solutions were performed under identical conditions (Figure S1). To ensure that the spectroelectrochemical experiments were performed under anaerobic conditions, a leak test performed with reduced methyl viologen (Figure S2).

**Resonance Raman Spectroscopy.** Resonance Raman (RR) spectra were collected with 364 nm excitation at room temperature from samples contained within a 1 cm x 1 cm

screw cap quartz cuvette (Starna Cells, Atascadero, CA), equipped with a gas-tight septum and a miniature stir bar. As with absorption spectroelectrochemistry, the electrodes used were pierced through the septum cap and immersed in solution. A miniature cuvette stir plate was taped to the bottom of the cuvette to agitate the solution and avoid photodamage. The resonance Raman instrumentation used has been described previously, with adjustments made for this particular sample cell.<sup>32</sup> Raman signal intensity was optimized and calibrated using known vibrational frequencies from a 1:1 v/v toluene:acetonitrile standard.<sup>33</sup> The band pass and accuracy were found to be  $10\text{ cm}^{-1}$  and  $\pm 1\text{ cm}^{-1}$ , respectively (Figure S3). Spectra of each sample were collected in one-minute signal integration increments over a total time frame of 80 minutes (30 min before electrolysis, 20 min during constant-potential electrolysis, 30 min after electrolysis under atmospheres of  $\text{N}_2$ ,  $\text{CO}_2$ , and  $\text{CO}$ ). Control samples of  $\text{NiCl}_2 \cdot 6\text{H}_2\text{O}$  and electrolyte buffer were obtained under the same conditions as the sample experiment (Figures S4-S5). Single-pixel spikes due to cosmic rays impinging on the detector were removed manually. Features from the phosphate buffer were subtracted from the spectra of  $[\text{Ni}(\text{cyclam})]^{2+}$  and a spline baseline was used to remove a broad fluorescent background. The summed spectra of  $[\text{Ni}(\text{cyclam})]^{2+}$  before electrolysis were subtracted directly from the spectra of  $[\text{Ni}(\text{cyclam})]^{2+}$  obtained during electrolysis to isolate peaks originating from the electrochemical process (Figures S6-S8).

**Electron Paramagnetic Resonance Spectroscopy.** All spectra were collected using a continuous-wave (CW) X-band EPR (EMX Plus, Bruker BioSpin, Billerica, MA) equipped with a Bruker Variable Temperature Unit (VTU). 150  $\mu\text{L}$  samples were removed via syringe from gas-tight scintillation vials or cuvettes following a 20-minute electrolysis experiment at a given potential and transferred to a septum-sealed EPR tube (4 mm OD, 3 mm ID, QSI, Fairport, OH) under  $\text{N}_2$  and Ar. The sample was frozen in liquid nitrogen within two minutes of the sample being removed from the electrolysis cell. Spectra were acquired for approximately ten minutes at 100-130 K using a microwave power of 20 mW, a modulation frequency of 100 kHz, and modulation amplitude of 10 G. One-to-one subtraction of the spectrum of a non-electrolyzed sample removed signals from the EPR cavity, and a residual broad, sloping baseline was removed using a spline subtraction. Spin quantitation of samples was performed using double-integration of the collected EPR spectra measured against a 240  $\mu\text{M}$  Cu(II) azurin spin standard. Spectra of control samples from electrolysis of nickel salts and electrolyte were also measured (Figure S9-S10). Spectral simulations were performed using the EasySpin toolbox (v. 5.2.14)<sup>34</sup> within the MATLAB (V. R2017b) software package.

**Gas Chromatography.** All gas chromatography analysis was performed on a Shimadzu GC-2014 fuel cell analyzer system. For each data point, a 150- $\mu\text{L}$  injection was removed from the sample headspace. Quantitation of carbon monoxide and hydrogen production utilized a flame ionization detector (FID) coupled to a methanizer and thermal conductivity detector (TCD), respectively. Argon was used as the carrier gas. Separation was achieved with the following columns: HayeSep-N (3 m, 80/100 mesh), HayeSep-T (2 m, 80/100 mesh), Shimalite Ångström molecular sieve (2.5 m, 60/80). Quantitative analysis of gas produced was determined by comparison against a standard curve (Figure S11-S12) generated from injections (50

$\mu\text{L}$  - 2.5 mL) of a Scotty standard gas calibration mixture (Plumsteadville, PA).

**DFT Calculations.** All calculations were performed using the ORCA quantum chemical computational package<sup>35</sup> on the Ohio Supercomputer Center.<sup>36</sup>  $[\text{Ni}(\text{cyclam})]$  models in both the *trans-I* and *trans-III* conformations were constructed using previously published structures of  $[\text{Ni}(\text{cyclam})]^{2+}$ <sup>21,37</sup> and modifying the charge and multiplicity to reflect the appropriate oxidation and spin state. Axial ligands were added manually in Chemcraft<sup>38</sup> prior to geometry optimization calculations, which were performed in the gas-phase without geometric constraints for energy minimization. All DFT calculations were performed using the B3LYP functional with the RIJCOSX approximation applied.<sup>39</sup> Relativistic effects were treated using the ZORA-def2-TZVP basis set on all carbon and hydrogen atoms and the ZORA-def2-TZVPP basis set on the nickel center as well as all directly coordinated atoms.<sup>40</sup> The geometry-optimized models were used for calculating optical excitations using time-dependent DFT (TD-DFT), EPR g-tensors, spin densities, hyperfine couplings, molecular orbitals, and vibrational frequencies.<sup>41-43</sup> TD-DFT transitions and extinction coefficients were calculated using the orca\_mapspc module and absorption spectra were generated through convolution with a Gaussian function of  $2500\text{ cm}^{-1}$  linewidth. The electronic difference densities of the high intensity transitions were visualized using the orca\_plot toolbox and select transitions were selected for calculating resonance Raman (RR) spectra using the orca\_asa module.<sup>44</sup> The calculated RR spectra were convolved with a  $10\text{ cm}^{-1}$  FWHM Gaussian linewidth for better comparison to experiment.

## Results

**Solution Electrochemistry of [1] Shows Atmosphere-Dependent Behavior.** Cyclic voltammetry was used for initial characterization of [1] under the selected experimental conditions (Figure S13). In aqueous, buffered solution under a nitrogen atmosphere, the  $\text{Ni}^{\text{II/I}}$  couple of [1] is masked by high levels of background proton reduction catalyzed by both [1] and the glassy carbon electrode at -1.1 V vs. NHE. This problem is further exacerbated when an amorphous graphite electrode is used (Figure S13). Under a  $\text{CO}_2$  atmosphere, electrocatalytic reduction of  $\text{CO}_2$  by [1] is also observed at approximately -1.1 V versus NHE. Because a non-catalytic signal is absent, the electrochemical turnover frequency under these conditions cannot be determined, though prior reports provide an estimate of  $0.5\text{ min}^{-1}$  with a mercury working electrode<sup>9,23</sup> and  $90\text{ s}^{-1}$  with a carbon working electrode.<sup>10</sup> A decrease in current and an anodic shift in peak position is observed under an atmosphere of  $\text{CO}$ , suggestive of  $\text{CO}$  binding to the reduced metal center and inhibition of catalysis. Consistent with this hypothesis, an anodic peak at approximately -0.4 V is observed, which may reflect oxidation of a  $\text{Ni}^{\text{I-CO}}$  species.<sup>22</sup>

**Electrocatalytic Activity and Selectivity is Electrode-Dependent.** Given the differences seen in the cyclic voltammograms, bulk electrolysis experiments using an amorphous graphite rod (AG) and a large surface area, glassy carbon (GC) electrode were coupled to gas chromatography analysis (GCA) to investigate the effects of electrode material on activity and selectivity (Figure 1 and Table ST1). From -0.7 V to -1.0 V vs. NHE, negligible activity is observed, with only

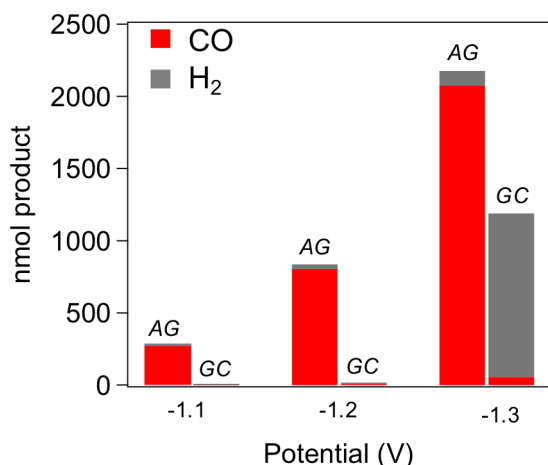


**Figure 1.** Gas chromatography analysis of products generated by electrolysis of [1] under a CO<sub>2</sub> atmosphere at varying potentials. Electrolysis was performed using an AG or GC working electrode as indicated.

baseline levels of CO and H<sub>2</sub> produced under all conditions. However, at potentials lower than -1.0 V vs. NHE, both H<sub>2</sub> and CO were observed, with values that increase significantly as the potential is lowered. Interestingly, despite being used in recent electrochemical studies on [1] in water mixtures, in our hands the GC electrode showed poor selectivity for CO<sub>2</sub> reduction, producing large quantities of H<sub>2</sub> and only small amounts of CO at low potentials.<sup>10,22</sup> The AG electrode showed strikingly different behavior. Specifically, the selectivity ratio (SR), defined as the amount of CO produced divided by the amount of H<sub>2</sub> generated, changed from ~0.2 for the GC electrode to over 20 for the AG electrode, with potential-independent values measured for electrolysis from -1.1 to -1.3 V vs. NHE. The SR values for the GC electrode are similar to those observed previously for light-driven, solution-phase CO<sub>2</sub> reduction by [1]<sup>45–47</sup>, while the increased selectivity of the AG electrode approaches that seen for electrolysis using a mercury cathode.<sup>37,48,49</sup> The control experiments performed in the absence of [1] show low background levels of CO and high levels of H<sub>2</sub> generated at low potentials (Tables ST2–ST3). The Faradaic efficiencies were also observed to be higher for the AG electrode (~45%) relative to the GC electrode (~2%), though the overall charge passed was approximately equivalent (Table

ST1). In the absence of CO<sub>2</sub>, large amounts of H<sub>2</sub> were generated by [1] with both electrodes (Table ST2).

**Optical Spectroelectrochemistry Reveals a Common Species Under Different Atmospheres.** To understand the molecular basis for the selectivity seen during CO<sub>2</sub> reduction by [1] using an AG electrode, optical spectra were measured under catalytic conditions for [1] under inert gas (N<sub>2</sub>) and in the presence of either substrate (CO<sub>2</sub>) or product (CO). These spectra were obtained by performing electrolysis experiments in a cuvette within the UV-Vis spectrometer. The resting state of [1] has a weak absorption feature at 450 nm ( $\epsilon_{450\text{ nm}} = 30\text{ M}^{-1}\text{ cm}^{-1}$ ) that can be attributed to forbidden d-d transitions, with no other pronounced features across the UV-visible region (Figure 2A).<sup>11</sup> During electrolysis at -1.3 V vs. NHE, broad visible and near-UV optical features become evident, with absorption maxima at 280 nm, 370 nm, and a shoulder at 400 nm (Figure 2A). This species is observed during electrolysis under N<sub>2</sub>, CO<sub>2</sub>, and CO, suggesting it is independent of the presence of either substrate or product (Figure S14). The extinction coefficient of this band at 370 nm is estimated to be approximately  $6250 \pm 500\text{ M}^{-1}\text{ cm}^{-1}$  through parallel optical and EPR spectroelectrochemical experiments (*vide infra*, Figure S15). Similar features are apparent during electrolysis with a GC electrode, albeit with lower intensities (Figure S16). Control experiments show that this species is not formed in samples with only Ni<sup>II</sup> salts or electrolyte alone (Figure S1), though electrolyte degradation following prolonged electrolysis under N<sub>2</sub> or CO contributes to the appearance of an absorption feature at 293 nm (Figure S17). **Resonance Raman Spectroscopy Provides Structural Information on the Reduced Species.** To gain insight into the molecular structure of the species giving rise to the new absorption feature at 370 nm, spectroelectrochemical resonance Raman spectroscopy was performed in the presence of N<sub>2</sub>, CO<sub>2</sub>, and CO (Figure 2B). Direct subtraction of the spectra of [1] before electrolysis from those obtained during and after electrolysis was used to isolate bands that resulted from the electrochemical process (Figure S6–S8). Features that increase as a result of electrochemical reduction are pronounced in the low- and mid-frequency regions of the spectra, with bands seen at 238, 345, 378, 448, 528, 823, 900, 1042, 1075, 1263, 1307, and 1358 cm<sup>-1</sup>. As with the optical spectroelectrochemical experiments, these bands seem to be unaffected by the nature of the gas present, though spin quantitation of a parallel experiment reveals concentrations of the metal-based signals to be 450  $\mu\text{M}$ , 210  $\mu\text{M}$ , and 170  $\mu\text{M}$  for experiments performed

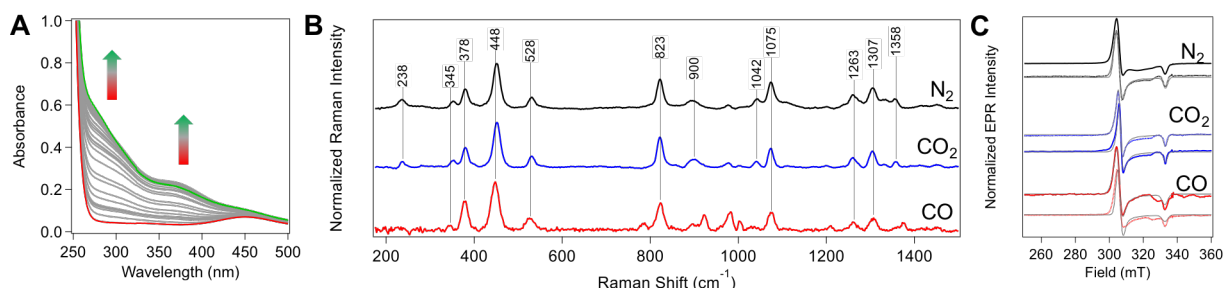


**Figure 2.** (A) Optical spectroelectrochemistry of 1.2 mM [Ni(cyclam)]<sup>2+</sup> before (red), during (grey), and after (green) 60 min. of electrolysis. Spectra were recorded every minute. (B) Resonance Raman spectra ( $\lambda_{\text{ex}} = 364\text{ nm}$ ) and (C) X-band EPR spectra of 1.2 mM [Ni(cyclam)]<sup>2+</sup> after 20 min. of electrolysis at -1.3 V (solid lines) or +1.2 V (dotted lines) vs. NHE under an N<sub>2</sub> (black), CO<sub>2</sub> (blue), or CO (red) atmosphere. Samples were prepared in 50 mM phosphate buffer, pH 7.0. Signal intensities were normalized to the height of the RR band at 448 cm<sup>-1</sup> and the EPR low-field turning point. Simulations for each EPR spectrum are overlaid (thin grey traces).

under N<sub>2</sub>, CO<sub>2</sub>, and CO, respectively. The bands between 300–500 cm<sup>-1</sup> are found in an energy range typical of metal-nitrogen single bonds. The higher frequency bands must include significant N-C or N-H motion. This suggests mixing of the metal-ligand and ligand-centered vibrational modes. Alternatively, the observation of these strong bands in the resonance Raman spectra may indicate some delocalization of the excited state onto the amine ligand framework, as these modes are not expected to be observed without resonance enhancement.<sup>50</sup> To resolve whether significant solvent or exchangeable proton motion is involved in any of the vibrational modes observed, experiments were run in deuterated buffers. Interestingly, the signal intensities were significantly lower in D<sub>2</sub>O (Figure S18). In addition, the frequencies of several modes are seen to change. Many bands shift to lower frequencies, including those at 452, 1075, 1263, and 1307 cm<sup>-1</sup>, while bands at 380, 528, and 823 cm<sup>-1</sup> shift to higher frequencies. This is indicative of hydrogen bonding interactions, which can result in frequencies that are observed to be at higher energies for the heavier isotope due to differences in hydrogen bond strength between protium and deuterium.<sup>51</sup>

**Electron Paramagnetic Resonance Spectra Indicate a Low-Spin Ni<sup>III</sup> Species is Formed.** Further characterization of the species generated by reductive electrolysis was obtained using EPR spectroscopy. Samples were measured after 20 minutes of electrolysis at potentials from -0.7 to -1.3 V vs. NHE, as well as after the spectroelectrochemical RR experiment (Figure 2C). Low concentrations of a metal-centered, EPR-active species are seen from -0.7 to -1.1 V (Figure S19–21), with increasing amounts generated by electrolysis at -1.2 and -1.3 V (Figure S19–21). Again, only minor spectral differences are observed between samples electrolyzed under N<sub>2</sub>, CO<sub>2</sub>, and CO. The approximately axial signal suggests a high degree of symmetry, while principal *g*-tensor values at 2.21, 2.17, and 2.02 are indicative of a SOMO with significant spin-orbit coupling. Collectively, these observations are consistent with an octahedral or square-pyramidal nickel(III)-based species (Figure S22).<sup>52,53</sup> At the most negative potentials, additional, low-intensity spectral features are observed on top of the primary Ni signal, suggesting a minority species is generated. However, attempts to clearly resolve these features were unsuccessful and may simply indicate the presence of a degradation product, consistent with observations in the UV-Vis spectroelectrochemical experiments (Figure S17). Control experiments performed with buffer, electrolyte, and NiCl<sub>2</sub> under the same electrolysis conditions exhibited no pronounced or metal-centered EPR signal.

**Electrolysis at Positive Potentials Shows the Same Nickel-Centered Species.**

To characterize additional electrochemically accessible nickel cyclam-based species, spectroelectrochemical experiments were also performed at +1.2 V vs. NHE. This anodic potential is sufficient to generate [Ni(cyclam)]<sup>3+</sup> (Figure S23), as evidenced by prior cyclic voltammetry experiments.<sup>6</sup> As with the low-potential experiments, the optical spectra also show an absorption feature at 370 nm that grows in with time during electrolysis (Figure S24). This band is not present in control experiments, suggesting it derives from [1]. The similarity in optical spectra led us to pursue RR spectroelectrochemistry under similar conditions. Surprisingly, the electrolysis product of [1] shows the same RR bands at +1.2 V vs. NHE as at -1.3 V vs. NHE (Figure S25)! This holds true across the different gas

atmospheres investigated. A parallel observation is made with EPR spectroscopy. Collectively, these results indicate that the species observed at reducing potentials is the same species that is generated under oxidative conditions. This suggests that Ni<sup>III</sup> is present during conditions that support either proton or CO<sub>2</sub> reduction (Figure S26).

An additional control experiment confirms that the oxidation state of the nickel-centered EPR-active species is +3. An aliquot of dithionite, which has a potential of -0.66 V at pH 7, was added to a sample of [Ni(cyclam)]<sup>2+</sup> following electrolysis at -1.3 V.<sup>54</sup> While this potential is not sufficient to reduce [Ni(cyclam)]<sup>2+</sup> to [Ni(cyclam)]<sup>+</sup>, the EPR signal that was originally measured was observed to disappear, consistent with the presence of a Ni<sup>III</sup> species (Figure S27).

**Phosphate Binding to [1] Traps the Ni<sup>III</sup> State.** To investigate the nature of the axial ligand bound to the Ni<sup>III</sup> species, the electrolyte and buffer were varied. Spectroelectrochemical experiments on a nickel cyclam compound that was synthesized with a sulfate counterion ([Ni<sup>III</sup>(cyclam)]SO<sub>4</sub>, [2]) in the presence of a perchlorate electrolyte showed the same optical, vibrational, and EPR features as those synthesized with chloride and run in a KCl electrolyte, indicating that the signals are unlikely to originate from a Cl<sup>-</sup>-bound species (Figure S28). On the other hand, experiments performed on [1] in sulfonate-containing Goods' buffers, MOPS and PIPES, at the same pH exhibited no optical signals during electrolysis at -1.3 V vs. NHE (Figure S29). GCA following 20 minutes of electrolysis of [1] in MOPS and PIPES buffers at -1.3 V vs. NHE showed similar levels of CO generated as in phosphate buffer, albeit with slightly weaker selectivity for CO over H<sub>2</sub> (Table ST1). Thus, phosphate was suggested to be critical not for activity, but for generating the trapped Ni<sup>III</sup> species. To probe the interaction between [1] and phosphate, the Ni<sup>III/II</sup> reduction potential was monitored as a function of phosphate concentration, revealing a relative binding affinity of phosphate to [Ni(cyclam)]<sup>3+</sup> of 7 × 10<sup>3</sup> M<sup>-1</sup> at pH 7 (Figure S30). This suggests that, in the 50 mM phosphate buffer used for the electrolysis experiments, phosphate binding is likely to occur if [Ni(cyclam)]<sup>3+</sup> is generated. Thus, the species generated and spectroscopically characterized from both reductive and oxidative electrolysis is suggested to be [Ni<sup>III</sup>(cyclam)(H<sub>x</sub>PO<sub>4</sub>)]<sup>x+</sup>.

GCA and EPR experiments performed under a CO atmosphere, which is known to inhibit CO<sub>2</sub> reduction by [1], indicate an initial correlation between the amount of H<sub>2</sub> produced and the concentration of Ni<sup>III</sup> observed in EPR, though further electrolysis simply increases the concentration of Ni<sup>III</sup> without resulting in greater amounts of H<sub>2</sub>. This data supports the hypothesis that the Ni<sup>III</sup> species is generated as an inhibitory side product during H<sup>+</sup> reduction (Figure S31). Electrolysis at negative potentials in the presence of oxygen also generates a similar optical signal at 370 nm (Figure S14). However, an induction period is observed, which may reflect O<sub>2</sub> reduction by the electrode prior to generation of [Ni(cyclam)]<sup>+</sup> and initiation of catalysis. The delayed appearance of the band at 370 nm when O<sub>2</sub> is present suggests that the Ni<sup>III</sup> species identified is not simply the result of oxygen reacting with the reduced nickel center.

**Computational Studies Support the Assignment of a [Ni(cyclam)(H<sub>2</sub>PO<sub>4</sub>)]<sup>2+</sup> Species.** Computational studies were used to confirm the protonation state and RR spectral assignments of the [Ni(cyclam)]<sup>3+</sup> species. Because there are multiple known conformational isomers of [1], computational models for

ARTICLE

me

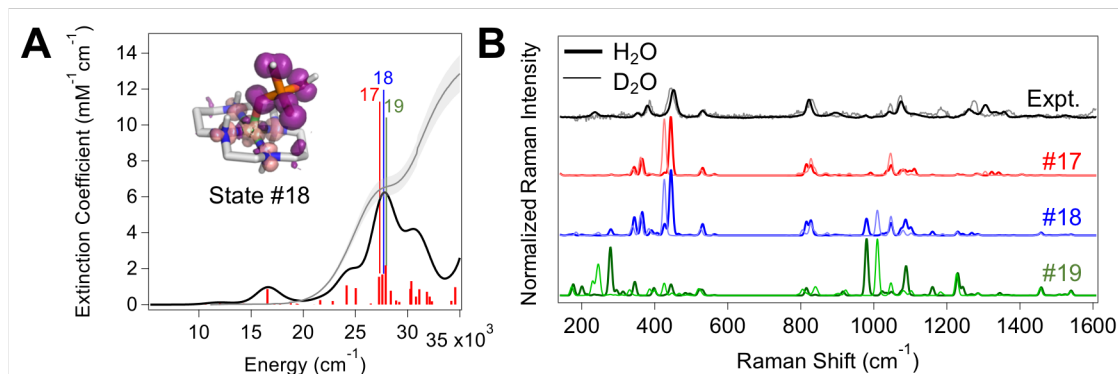


**Figure 3.** (A) TD-DFT calculated absorption spectra of  $[\text{Ni}(\text{cyclam})(\text{H}_2\text{PO}_4)]^{2+}$  (grey) overlaid with the experimental UV-Vis spectrum of electrochemically reduced  $[\text{Ni}(\text{cyclam})]^{2+}$  (black). (Inset) Structure of  $[\text{Ni}(\text{cyclam})(\text{H}_2\text{PO}_4)]^{2+}$  shown with transition difference density (positive density shown in pink, negative density shown in purple) for State 18 (indicated). (B) Comparison of normalized experimental resonance Raman spectra of **[1]** following electrolysis at -1.3 V vs. NHE under  $\text{N}_2$  in  $\text{H}_2\text{O}$  (black) and  $\text{D}_2\text{O}$  (grey) with calculated resonance Raman spectra of  $[\text{Ni}(\text{cyclam})(\text{H}_2\text{PO}_4)]^{2+}$  shown for States 17 (red), 18 (blue), and 19 (green) in  $\text{H}_2\text{O}$  (thick lines) overlaid with spectra calculated for deuterated samples (thin lines). Calculated resonance Raman spectra of each species used an excitation energy of  $27,472\text{ cm}^{-1}$  and were convolved with a  $10\text{ cm}^{-1}$  Gaussian linewidth.

possible intermediates in the catalytic cycle for  $\text{CO}_2$  and  $\text{H}^+$  reduction by **[1]** were considered in the trans-I and trans-III conformations for both the  $\text{Ni}^{\text{I}}$  and  $\text{Ni}^{\text{III}}$  oxidation states.<sup>21,31,55,56</sup>

In addition, the aqueous, buffered nature of the electrolysis solution motivated the construction of  $\text{Ni}^{\text{III}}$  models that incorporated either one or two water, hydroxide, hydride, or phosphate ligands bound to the axial sites. Energy-minimized structures revealed no significant changes in geometry of the cyclam ring upon coordination of each of the ligands, and geometries converged properly (Table ST4).

From the optimized geometries, the observed spectroscopic properties could be calculated. The predicted g-tensors for each model considered are given in Table ST5. As expected from simple electronic structure and ligand field arguments, structures with a  $\text{Ni}^{\text{I}}$  oxidation state show axial symmetry that is reversed from what is observed experimentally, with  $g_x = g_y < g_z$ . Although the calculated symmetry matches the experimental symmetry in the  $\text{Ni}^{\text{III}}$  oxidation state, a  $[\text{Ni}(\text{cyclam})]^{3+}$  species that lacks axial coordination from any exogenous ligands is predicted to exhibit g-values that deviate significantly from experiment for both conformations. Only the models featuring axial coordination from water or a monoanionic ligand in the trans-III conformation, which is known to be the majority conformation in solution,<sup>55</sup> result in g-values that agree with the experimental EPR spectra. Specifically, the model in which a single, monobasic phosphate anion ( $[\text{H}_2\text{PO}_4]^-$ ) is bound to the nickel center gives calculated g-values of 2.033, 2.176, and 2.177 that are most closely matched to experiment, with spin density primarily localized in the nickel  $d_{z^2}$  orbital.

A closer investigation of the favored models featuring axial coordination from water or a monoanionic ligand in the trans-III conformation using TD-DFT-calculated absorption and resonance Raman spectra was performed. The calculated absorption and resonance Raman spectra of the monobasic, phosphate-bound  $[\text{Ni}(\text{cyclam})(\text{H}_2\text{PO}_4)]^{2+}$  also provide the closest match to the experimental spectra (Figure 3 and S32-S36). The dominant bands in the near-UV are due to phosphate-to-nickel charge transfer states (Figure 3A, inset), with fairly good agreement between experiment and theory in both intensity and energy.<sup>57</sup> An absorption band at  $16,000\text{ cm}^{-1}$  is also calculated, predicted to be centered on a terminal phosphate hydroxyl moiety (Figure S37). However, these spurious, low-energy transitions are known to plague TD-DFT calculations on highly charged species or those with substantial charge-transfer

character, and significantly higher level calculations would be required to resolve this issue, which are beyond the scope of this work.<sup>44,58</sup> The prominent LMCT transitions provide strong resonance enhancement of the nickel-phosphate modes, with a pronounced symmetric stretch at  $839\text{ cm}^{-1}$  and asymmetric stretching modes at  $980$  and  $1090\text{ cm}^{-1}$  (Figure 3B). The low frequency bands at  $345$ ,  $365$ , and  $445\text{ cm}^{-1}$  can be attributed to ring-breathing modes coupled into the metal center. The calculated bands are predicted to shift upon deuteration to a degree that is largely consistent with experiment, both in the direction and magnitude of the calculated shifts, again with the greatest agreement seen for the  $[\text{Ni}(\text{cyclam})(\text{H}_2\text{PO}_4)]^{2+}$  model (Figure S38-S39).

Binding of the dibasic phosphate species to  $[\text{Ni}(\text{cyclam})]^{3+}$  was also considered. However, the calculated spectroscopic parameters for  $[\text{Ni}(\text{cyclam})(\text{HPO}_4)]^+$  deviated significantly from those observed experimentally (Figure S37 and Table S5). It is on this basis that the assignment of the phosphate-bound species to be  $[\text{Ni}(\text{cyclam})(\text{H}_2\text{PO}_4)]^{2+}$  is favored. Coordination of phosphate to the Lewis acidic metal center is likely to decrease the ligand  $\text{pK}_a$ , perturbing the protonation equilibria, though those effects are not easily quantified and have not been addressed in this work.

## Discussion

**Effects of Electrode Composition on Catalysis by [1].** The different product distributions and absolute activities seen with the GC and AG electrodes, the latter being more active and selective, may be attributed to two contributing factors. Greater basal levels of  $\text{H}^+$  reduction activity by the high surface area AG electrode may change the immediate environment by depleting local  $\text{H}^+$  concentration, resulting in higher local pH values around the catalyst.<sup>59</sup> This hypothesis is supported by the observation that control experiments performed in the absence of **[1]** also show greater amounts of  $\text{H}_2$  produced by electrolysis with an AG electrode (Table ST3). Interactions between **[1]** and the electrode surface or electrochemical double layer may also affect the catalytic behaviour.<sup>28,60</sup> Adsorption of **[1]** to mercury-based electrodes has been shown to increase specificity and activity, presumably by stabilizing the compound in an active conformation.<sup>9,23</sup> This selective stabilization<sup>11,45,48,61</sup> may also be occurring with the AG electrode, which is known to adsorb proteins and other cationic compounds.<sup>62-64</sup> However, because

the catalytic currents show a square-root dependence on scan rate (Figure S40), catalysis is suggested to occur through a diffusion-controlled, homogeneous process.<sup>52</sup> Thus, these surface-based interactions may be transient on the timescale of turnover.<sup>65,66</sup>

The low Faradaic efficiencies seen during catalysis may be due to the generation of side products.<sup>59,67–69</sup> Because the concentrations of [1] required for the spectroscopy experiments are much greater than those typically used in activity analysis, the absolute total turnover numbers of [1] are substoichiometric, indicating that only a small fraction of active species are generated. This is confirmed from spin quantification of the trapped Ni<sup>III</sup> species, which suggests only low amounts, approximately 10% of the starting [1] concentration, accumulate during electrolysis (Figure S19). Thus, the residual charge passed that does not promote CO or H<sub>2</sub> production may contribute to production of partially reduced [Ni(cyclam)] species or degradation of buffer and electrolyte, which becomes pronounced after extended electrolysis (Figure S41).

**Computational Studies Facilitate Molecular Identification of Observed Species.** To identify the species trapped and characterized using optical, vibrational, and EPR spectroscopy, DFT calculations provide a highly valuable complement to experiment. Consistent with prior reports on [Ni(cyclam)]<sup>1+</sup> in organic solvents, the EPR g-tensor calculations for all [Ni(cyclam)]<sup>+</sup> species in any conformation were strikingly inconsistent with experimental values.<sup>23</sup> Moreover, the observed EPR spectra are well-matched to those previously published for a chemically oxidized [Ni(cyclam)]<sup>3+</sup> species.<sup>53</sup> These observations support the assignment of the EPR-active species to a Ni<sup>III</sup> state, though the calculated g-values for a Ni<sup>III</sup>-H species are sufficiently different from those seen experimentally to tentatively rule out this species (Table S5). Because the calculated g-values for most of the other [Ni<sup>III</sup>(cyclam)(L)] species investigated show at least moderate agreement with the experimental values, even in the absence of coordinating ligands, CW X-band EPR is not sufficient to differentiate between four-coordinate [Ni(cyclam)]<sup>3+</sup> and five- and six-coordinate species.

The calculated optical and resonance Raman spectra provide additional constraints on identifying the nature of the species trapped in the electrochemical experiments. While the TD-DFT calculations indicate a near-UV charge-transfer transition would be seen for [Ni(cyclam)]<sup>3+</sup> bound to many of the proposed ligand permutations, including chloride, mono-, di-, and tribasic phosphate (Figure S32-S36), the resonance Raman spectra obtained with excitation into those transitions vary drastically across the different species (Figure S38). These differences between experiment and theory are further exacerbated when isotope shifts for exchangeable protons were considered and compared to experimental samples prepared in deuterated buffers (Figures S38-S39). Models containing a Ni<sup>III</sup>-hydride state as well as those with bis-hydroxide, mono- and bis-chloride, bis-phosphate ligands, one or two aquo ligands, and a single hydroxide ligand were ruled out on this basis. Thus, the only calculated configuration that gave reasonable agreement with all three spectroscopic observables, including the magnitude and direction of the isotope shifts seen, is [Ni<sup>III</sup>(cyclam)] bound to a single, monobasic phosphate ligand.

**Implications for the Mechanism of H<sup>+</sup> Reduction by [1] and Design of Selective Catalysts for CO<sub>2</sub> Reduction.** The

spectroelectrochemical experiments at reducing potentials were intended to trap and characterize reduced [Ni(cyclam)]<sup>1+</sup> or a catalytically relevant substrate- or product-bound state. However, the species that appears during electrolysis is found instead to be a [Ni<sup>III</sup>(cyclam)(H<sub>2</sub>PO<sub>4</sub>)]<sup>2+</sup> species, trapped as a side product in low concentrations during H<sup>+</sup> reduction. The nickel oxidation state has been verified through analogous experiments at high potentials and the quenching of the EPR signal upon addition of dithionite. It is likely that complete electrolytic reduction of the Ni<sup>III</sup> species does not occur because of rapid diffusion away from the electrode, as the solutions are vigorously stirred, in conjunction with the high binding affinity of the phosphate ligand to a Ni<sup>III</sup> center.

Though the compound trapped is an inhibited state, the observation of a Ni<sup>III</sup> species at reducing potentials under N<sub>2</sub> in an aqueous solution indicates that [1] must pass through the Ni<sup>III</sup> oxidation state during catalysis. This implies an ECCE mechanism is dominant for H<sup>+</sup> reduction and suggests that [Ni(H)(cyclam)]<sup>2+</sup> may be the active species in H<sub>2</sub> generation (Scheme 1). As such, the proposed mechanism for hydrogen production by [1] differs both from previously proposed mechanisms for H<sub>2</sub> production and from the proposed mechanism for CO<sub>2</sub> reduction by [1].<sup>21</sup> However, there are other known H<sub>2</sub> production catalysts that are predicted to follow an ECCE mechanism.<sup>70–73</sup>

The importance of knowing the basic mechanisms for CO<sub>2</sub> reduction and H<sub>2</sub> production by [1] can facilitate the design of more efficient and selective catalysts. For example, developing catalysts that destabilize a Ni<sup>III</sup> species may disfavor proton reduction, a hypothesis that is currently being explored in our lab. Additionally, the differential activity seen across the two carbon-based electrodes and the observation of trapped, buffer-bound species highlights the importance of carefully considering all experimental conditions, including buffer identity, pH, supporting electrolyte, and working electrode, when benchmarking and characterizing new catalysts.

## Conclusions

This work reports on the observation of a solvated [Ni<sup>III</sup>(cyclam)] species trapped at reducing potentials, which indicates that an ECCE mechanism is active for H<sup>+</sup> reduction by [1]. This is different from the ECEC mechanism proposed for electrocatalytic CO<sub>2</sub> reduction by [Ni(cyclam)]<sup>2+</sup>. The insight gained by identifying the pathway for hydrogen production can be used to enhance selectivity for CO<sub>2</sub> reduction by manipulating conditions or installing catalyst modifications that destabilize this Ni<sup>III</sup> state. This approach can bias the reaction towards an ECEC pathway for CO<sub>2</sub> reduction.

## Conflicts of interest

There are no conflicts to declare.

## Acknowledgements

The authors would like to acknowledge the Turro group for generously allowing the use of their rotary evaporator. The authors would like to acknowledge the National Science Foundation (CHE-1454289) and Department of Energy (EC DE-SC0018020) for financial support of this project. We would like

to also acknowledge computational resources from the Ohio Supercomputer Center (PAS-1001).

## Notes and references

- Sawyer, J. S. Man-Made Carbon Dioxide and the "Greenhouse" Effect. *Nature* **1972**, *239* (5366), 23–26.
- Appel, A. M.; Bercaw, J. E.; Bocarsly, A. B.; Dobbek, H.; DuBois, D. L.; Dupuis, M.; Ferry, J. G.; Fujita, E.; Hille, R.; Kenis, P. J. A.; et al. Frontiers, Opportunities, and Challenges in Biochemical and Chemical Catalysis of CO<sub>2</sub> Fixation. *Chem. Rev.* **2013**, *113* (8), 6621–6658.
- Zimmermann, P.; Limberg, C. Activation of Small Molecules at Nickel(II) Moieties. *J. Am. Chem. Soc.* **2017**, *139* (12), 4233–4242.
- Sahoo, D.; Yoo, C.; Lee, Y. Direct CO<sub>2</sub> Addition to a Ni(0)–CO Species Allows the Selective Generation of a Nickel(II) Carboxylate with Expulsion of CO. *J. Am. Chem. Soc.* **2018**, *140* (6), 2179–2185.
- Yoo, C.; Kim, Y.-E.; Lee, Y. Selective Transformation of CO<sub>2</sub> to CO at a Single Nickel Center. *Acc. Chem. Res.* **2018**, *51* (5), 1144–1152.
- Schneider, J.; Jia, H.; Muckerman, J. T.; Fujita, E. Thermodynamics and Kinetics of CO<sub>2</sub>, CO, and H<sup>+</sup> Binding to the Metal Centre of CO<sub>2</sub> Reduction Catalysts. *Chem Soc Rev* **2012**, *41* (6), 2036–2051.
- Wang, J.-W.; Liu, W.-J.; Zhong, D.-C.; Lu, T.-B. Nickel Complexes as Molecular Catalysts for Water Splitting and CO<sub>2</sub> Reduction. *Coord. Chem. Rev.* **2017**.
- Meshitsuka, S.; Ichikawa, M.; Tamaru, K. Electrocatalysis by Metal Phthalocyanines in the Reduction of Carbon Dioxide. *J. Chem. Soc. Chem. Commun.* **1974**, *0* (5), 158–159.
- Beley, M.; Collin, J.-P.; Ruppert, R.; Sauvage, J.-P. Nickel(II)-Cyclam: An Extremely Selective Electrocatalyst for Reduction of CO<sub>2</sub> in Water. *J. Chem. Soc., Chem. Commun.* **1984**, No. 19, 1315–1316.
- Froehlich, J. D.; Kubiak, C. P. Homogeneous CO<sub>2</sub> Reduction by Ni(Cyclam) at a Glassy Carbon Electrode. *Inorg. Chem.* **2012**, *51* (7), 3932–3934.
- Craig, C. A.; Spreer, L. O.; Otvos, J. W.; Calvin, M. Photochemical Reduction of Carbon Dioxide Using Nickel Tetraazamacrocycles. *J. Phys. Chem.* **1990**, *94* (20), 7957–7960.
- Schneider, C. R.; Shafaat, H. S. An Internal Electron Reservoir Enhances Catalytic CO<sub>2</sub> Reduction by a Semisynthetic Enzyme. *Chem. Commun.* **2016**, *52* (64), 9889–9892.
- Zilbermann, I.; Maimon, E.; Cohen, H.; Meyerstein, D. Redox Chemistry of Nickel Complexes in Aqueous Solutions. *Chem. Rev.* **2005**, *105* (6), 2609–2626.
- Shamir, D.; Zilbermann, I.; Maimon, E.; Shames, A. I.; Cohen, H.; Meyerstein, D. Anions as Stabilizing Ligands for Ni(III)(Cyclam) in Aqueous Solutions. *Inorganica Chim. Acta* **2010**, *363* (12), 2819–2823.
- Schneider, C. R.; Manesis, A. C.; Stevenson, M. J.; Shafaat, H. S. A Photoactive Semisynthetic Metalloenzyme Exhibits Complete Selectivity for CO<sub>2</sub> Reduction in Water. *Chem. Commun.* **2018**, *54* (37), 4681–4684.
- Sommer, D. J.; Vaughn, M. D.; Ghirlanda, G. Protein Secondary-Shell Interactions Enhance the Photoinduced Hydrogen Production of Cobalt Protoporphyrin IX. *Chem. Commun.* **2014**, *50* (100), 15852–15855.
- Lu, Y.; Yeung, N.; Sieracki, N.; Marshall, N. M. Design of Functional Metalloproteins. *Nature* **2009**, *460* (7257), 855–862.
- Sohtau, S. R.; Dahlberg, P. D.; Niklas, J.; Poluektov, O. G.; Mulfort, K. L.; Utschig, L. M. Ru–Protein–Co Biohybrids Designed for Solar Hydrogen Production: Understanding Electron Transfer Pathways Related to Photocatalytic Function. *Chem. Sci.* **2016**, *7* (12), 7068–7078.
- Akhade, S. A.; Luo, W.; Nie, X.; Bernstein, N. J.; Asthagiri, A.; Janik, M. J. Poisoning Effect of Adsorbed CO during CO<sub>2</sub> Electroreduction on Late Transition Metals. *Phys Chem Chem Phys* **2014**, *16* (38), 20429–20435.
- Hori, Y.; Wakebe, H.; Tsukamoto, T.; Koga, O. Electrocatalytic Process of CO Selectivity in Electrochemical Reduction of CO<sub>2</sub> at Metal Electrodes in Aqueous Media. *Electrochimica Acta* **1994**, *39* (11), 1833–1839.
- Song, J.; Klein, E. L.; Neese, F.; Ye, S. The Mechanism of Homogeneous CO<sub>2</sub> Reduction by Ni(Cyclam): Product Selectivity, Concerted Proton-Electron Transfer and C–O Bond Cleavage. *Inorg. Chem.* **2014**, *53* (14), 7500–7507.
- Froehlich, J. D.; Kubiak, C. P. The Homogeneous Reduction of CO<sub>2</sub> by [Ni(Cyclam)]<sup>+</sup>: Increased Catalytic Rates with the Addition of a CO Scavenger. *J. Am. Chem. Soc.* **2015**, *137* (10), 3565–3573.
- Beley, M.; Collin, J. P.; Ruppert, R.; Sauvage, J. P. Electrocatalytic Reduction of Carbon Dioxide by Nickel Cyclam<sup>2+</sup> in Water: Study of the Factors Affecting the Efficiency and the Selectivity of the Process. *J. Am. Chem. Soc.* **1986**, *108* (24), 7461–7467.
- Fisher, B. J.; Eisenberg, R. Electrocatalytic Reduction of Carbon Dioxide by Using Macrocycles of Nickel and Cobalt. *J. Am. Chem. Soc.* **1980**, *102* (24), 7361–7363.
- Waldie, K. M.; Brunner, F. M.; Kubiak, C. P. Transition Metal Hydride Catalysts for Sustainable Interconversion of CO<sub>2</sub> and Formate: Thermodynamic and Mechanistic Considerations. *ACS Sustain. Chem. Eng.* **2018**, *6* (5), 6841–6848.
- Waldie, K. M.; Ostericher, A. L.; Reineke, M.; Sasayama, A. F.; Kubiak, C. P. Hydrity of Transition Metal Hydrides: Thermodynamic Considerations for CO<sub>2</sub> Reduction. *ACS Catal.* **2017**.
- Vyskočil, V.; Barek, J. Mercury Electrodes—Possibilities and Limitations in Environmental Electroanalysis. *Crit. Rev. Anal. Chem.* **2009**, *39* (3), 173–188.
- Izzet, K.; Ghanem, M.; Al-Mayouf, A.; Alhoshan, M.; Bartlett, P. A Study of the Modification of Glassy Carbon and Edge and Basal Plane Highly Oriented Pyrolytic Graphite Electrodes Modified with Anthraquinone Using Diazonium Coupling and Solid Phase Synthesis and Their Use for Oxygen Reduction. *J. Electroanal. Chem.* **2013**, *706*, 25–32.
- Yuan, W.; Zhou, Y.; Li, Y.; Li, C.; Peng, H.; Zhang, J.; Liu, Z.; Dai, L.; Shi, G. The Edge- and Basal-Plane-Specific Electrochemistry of a Single-Layer Graphene Sheet. *Sci. Rep.* **2013**, *3*, 2248.
- Kelly, C. A.; Mulazzani, Q. G.; Blinn, E. L.; Rodgers, M. A. J. Kinetics of CO Addition to Ni(Cyclam)<sup>+</sup> in Aqueous Solution. *Inorg. Chem.* **1996**, *35* (18), 5122–5126.
- Bosnich, B.; Tobe, M. L.; Webb, G. A. Complexes of Nickel(II) with a Cyclic Tetradentate Secondary Amine. *Inorg. Chem.* **1965**, *4* (8), 1109–1112.
- Slater, J. W.; Marguet, S. C.; Cirino, S. L.; Maugeri, P. T.; Shafaat, H. S. Experimental and DFT Investigations Reveal the Influence of the Outer Coordination Sphere on the

- Vibrational Spectra of Nickel-Substituted Rubredoxin, a Model Hydrogenase Enzyme. *Inorg. Chem.* **2017**, *56* (7), 3926–3938.
- (33) McCreery, R. L. *Raman Spectroscopy for Chemical Analysis*; Chemical analysis; Wiley: New York, 2000.
- (34) Stoll, S.; Schweiger, A. EasySpin, a Comprehensive Software Package for Spectral Simulation and Analysis in EPR. *J. Magn. Reson.* **2006**, *178* (1), 42–55.
- (35) Neese, F. The ORCA Program System: The ORCA Program System. *Wiley Interdiscip. Rev. Comput. Mol. Sci.* **2012**, *2* (1), 73–78.
- (36) *Ohio Supercomputer Center*; Ohio Supercomputer Center: Columbus, OH, 1987.
- (37) Neri, G.; J. Walsh, J.; Wilson, C.; Reynal, A.; C. Lim, J. Y.; Li, X.; P. White, A. J.; J. Long, N.; R. Durrant, J.; J. Cowan, A. A Functionalised Nickel Cyclam Catalyst for CO<sub>2</sub> Reduction: Electrocatalysis, Semiconductor Electron Transfer. *Phys. Chem. Chem. Phys.* **2015**, *17* (3), 1562–1566.
- (38) Chemcraft - Graphical program for visualization of quantum chemistry computations <https://www.chemcraftprog.com/> (accessed Apr 6, 2018).
- (39) Kossmann, S.; Neese, F. Efficient Structure Optimization with Second-Order Many-Body Perturbation Theory: The RIJCOSX-MP2 Method. *J. Chem. Theory Comput.* **2010**, *6* (8), 2325–2338.
- (40) Lenthe, E. van; Baerends, E. J.; Snijders, J. G. Relativistic Regular Two-component Hamiltonians. *J. Chem. Phys.* **1993**, *99* (6), 4597–4610.
- (41) Pantazis, D. A.; Chen, X.-Y.; Landis, C. R.; Neese, F. All-Electron Scalar Relativistic Basis Sets for Third-Row Transition Metal Atoms. *J. Chem. Theory Comput.* **2008**, *4* (6), 908–919.
- (42) Grimme, S.; Ehrlich, S.; Goerigk, L. Effect of the Damping Function in Dispersion Corrected Density Functional Theory. *J. Comput. Chem.* **2011**, *32* (7), 1456–1465.
- (43) Grimme, S.; Antony, J.; Ehrlich, S.; Krieg, H. A Consistent and Accurate Ab Initio Parametrization of Density Functional Dispersion Correction (DFT-D) for the 94 Elements H-Pu. *J. Chem. Phys.* **2010**, *132* (15), 154104.
- (44) Neese, F. Prediction of Molecular Properties and Molecular Spectroscopy with Density Functional Theory: From Fundamental Theory to Exchange-Coupling. *Coord. Chem. Rev.* **2009**, *253* (5), 526–563.
- (45) Neri, G.; M. Aldous, I.; J. Walsh, J.; J. Hardwick, L.; J. Cowan, A. A Highly Active Nickel Electrocatalyst Shows Excellent Selectivity for CO<sub>2</sub> Reduction in Acidic Media. *Chem. Sci.* **2016**, *7* (2), 1521–1526.
- (46) Tinnemans, A. H. A.; Koster, T. P. M.; Thewissen, D. H. M. W.; Mackor, A. Tetraaza-Macrocyclic Cobalt(II) and Nickel(II) Complexes as Electron-Transfer Agents in the Photo(Electro)Chemical and Electrochemical Reduction of Carbon Dioxide. *Recl. Trav. Chim. Pays-Bas* **1984**, *103* (10), 288–295.
- (47) Jubran, N.; Ginzburg, G.; Cohen, H.; Koresh, Y.; Meyerstein, D. Stabilization of the Monovalent Nickel Complex with 1,4,8,11-Tetraazacyclotetradecane in Aqueous Solutions by N- and C-Methylation. An Electrochemical and Pulse Radiolysis Study. *Inorg. Chem.* **1985**, *24* (3), 251–258.
- (48) Balazs, G. B.; Anson, F. C. The Adsorption of Ni(Cyclam)<sup>+</sup> at Mercury Electrodes and Its Relation to the Electrocatalytic Reduction of CO<sub>2</sub>. *J. Electroanal. Chem.* **1992**, *322* (1), 325–345.
- (49) Fujihira, M.; Hirata, Y.; Suga, K. Electrocatalytic Reduction of CO<sub>2</sub> by Nickel(II) Cyclam. *J. Electroanal. Chem. Interfacial Electrochem.* **1990**, *292* (1), 199–215.
- (50) Basile, L. J. Metal-Nitrogen Vibrations. In *Low-Frequency Vibrations of Inorganic and Coordination Compounds*; Springer, Boston, MA, 1971; pp 191–246.
- (51) Scheiner, S.; Čuma, M. Relative Stability of Hydrogen and Deuterium Bonds. *J. Am. Chem. Soc.* **1996**, *118* (6), 1511–1521.
- (52) Drago, R. S.; Drago, R. S. *Physical Methods for Chemists*, 2nd ed.; Saunders College Pub: Ft. Worth, 1992.
- (53) Telser, J. A Perspective on Applications of Ligand-Field Analysis: Inspiration from Electron Paramagnetic Resonance Spectroscopy of Coordination Complexes of Transition Metal Ions. *J. Braz. Chem. Soc.* **2006**, *17* (8), 1501–1515.
- (54) Mayhew, S. G. The Redox Potential of Dithionite and SO<sub>2</sub><sup>-</sup> from Equilibrium Reactions with Flavodoxins, Methyl Viologen and Hydrogen plus Hydrogenase. *Eur. J. Biochem.* **1978**, *85* (2), 535–547.
- (55) Maimon, E.; Zilbermann, I.; Cohen, H.; Kost, D.; van Eldik, R.; Meyerstein, D. Mechanism of Isomerization of Ni(Cyclam) in Aqueous Solutions. *Eur. J. Inorg. Chem.* **2005**, *2005* (24), 4997–5004.
- (56) Adam, K. R.; Atkinson, I. M.; Lindoy, L. F. Local Density Functional Theory Analysis of the Structures and Energies of the Isomers of Low-Spin [Ni(Cyclam)]<sup>2+</sup>. *Inorg. Chem.* **1997**, *36* (3), 480–481.
- (57) Neese, F. A Critical Evaluation of DFT, Including Time-Dependent DFT, Applied to Bioinorganic Chemistry. *J. Biol. Inorg. Chem. JBIC Publ. Soc. Biol. Inorg. Chem.* **2006**, *11* (6), 702–711.
- (58) Laurent, A. D.; Jacquemin, D. TD-DFT Benchmarks: A Review. *Int. J. Quantum Chem.* **2013**, *113* (17), 2019–2039.
- (59) Gattrell, M.; Gupta, N.; Co, A. A Review of the Aqueous Electrochemical Reduction of CO<sub>2</sub> to Hydrocarbons at Copper. *J. Electroanal. Chem.* **2006**, *594* (1), 1–19.
- (60) Ryu, J.; Wuttig, A.; Surendranath, Y. Quantification of Interfacial pH Variation at Molecular Length Scales Using a Concurrent Non-Faradaic Reaction. *Angew. Chem. Int. Ed.* **2018**, *57* (30), 9300–9304.
- (61) Wu, Y.; Rudshteyn, B.; Zhanaidarova, A.; Froehlich, J. D.; Ding, W.; Kubiak, C. P.; Batista, V. S. Electrode-Ligand Interactions Dramatically Enhance CO<sub>2</sub> Conversion to CO by the [Ni(Cyclam)](PF<sub>6</sub>)<sub>2</sub> Catalyst. *ACS Catal.* **2017**, *7* (8), 5282–5288.
- (62) Perreault, F.; Faria, A. F. de; Elimelech, M. Environmental Applications of Graphene-Based Nanomaterials. *Chem. Soc. Rev.* **2015**, *44* (16), 5861–5896.
- (63) Wang, K.; Zhou, C.; Hong, Y.; Zhang, X. A Review of Protein Adsorption on Bioceramics. *Interface Focus* **2012**, *2* (3), 259–277.
- (64) Sharma, P.; Das, M. R. Removal of a Cationic Dye from Aqueous Solution Using Graphene Oxide Nanosheets: Investigation of Adsorption Parameters. *J. Chem. Eng. Data* **2013**, *58* (1), 151–158.
- (65) Wuttig, A.; Yaguchi, M.; Motobayashi, K.; Osawa, M.; Surendranath, Y. Inhibited Proton Transfer Enhances Au-Catalyzed CO<sub>2</sub>-to-Fuels Selectivity. *Proc. Natl. Acad. Sci.* **2016**, *113* (32), E4585–E4593.
- (66) Wuttig, A.; Liu, C.; Peng, Q.; Yaguchi, M.; Hendon, C. H.; Motobayashi, K.; Ye, S.; Osawa, M.; Surendranath, Y.

- Tracking a Common Surface-Bound Intermediate during CO<sub>2</sub>-to-Fuels Catalysis. *ACS Cent. Sci.* **2016**, *2* (8), 522–528.
- (67) Santos, T. R. dos; Nilges, P.; Sauter, W.; Harnisch, F.; Schröder, U. Electrochemistry for the Generation of Renewable Chemicals: Electrochemical Conversion of Levulinic Acid. *RSC Adv.* **2015**, *5* (34), 26634–26643.
- (68) Hori, Y.; Konishi, H.; Futamura, T.; Murata, A.; Koga, O.; Sakurai, H.; Oguma, K. “Deactivation of Copper Electrode” in Electrochemical Reduction of CO<sub>2</sub>. *Electrochimica Acta* **2005**, *50* (27), 5354–5369.
- (69) Görlin, M.; Chernev, P.; Ferreira de Araújo, J.; Reier, T.; Dresch, S.; Paul, B.; Krähnert, R.; Dau, H.; Strasser, P. Oxygen Evolution Reaction Dynamics, Faradaic Charge Efficiency, and the Active Metal Redox States of Ni–Fe Oxide Water Splitting Electrocatalysts. *J. Am. Chem. Soc.* **2016**, *138* (17), 5603–5614.
- (70) Becker, R.; Amirjalayer, S.; Li, P.; Woutersen, S.; Reek, J. N. H. An Iron-Iron Hydrogenase Mimic with Appended Electron Reservoir for Efficient Proton Reduction in Aqueous Media. *Sci. Adv.* **2016**, *2* (1), e1501014.
- (71) Chong, D.; Georgakaki, I. P.; Mejia-Rodriguez, R.; Sanabria-Chinchilla, J.; Soriaga, M. P.; Darensbourg, M. Y. Electrocatalysis of Hydrogen Production by Active Site Analogues of the Iron Hydrogenase Enzyme: Structure/Function Relationships. *Dalton Trans* **2003**, *0*, 4158–4163.
- (72) Mejia-Rodriguez, R.; Chong, D.; Reibenspies, J. H.; Soriaga, M. P.; Darensbourg, M. Y. The Hydrophilic Phosphotriazaadamantane Ligand in the Development of H<sub>2</sub> Production Electrocatalysts: Iron Hydrogenase Model Complexes. *J. Am. Chem. Soc.* **2004**, *126* (38), 12004–12014.
- (73) Kochubey, D.; Kaichev, V.; Saraev, A.; Tomy, S.; Belov, A.; Voloshin, Y. Combined X-Ray Absorption Near-Edge Structure and X-Ray Photoelectron Study of the Electrocatalytically Active Cobalt(I) Cage Complexes and the Clathrochelate Cobalt(II)- and Cobalt(III)-Containing Precursors and Analogs. *J. Phys. Chem. C* **2013**, *117* (6), 2753–2759.

Characterization of a Ni<sup>III</sup> species during reductive catalysis by [Ni(cyclam)]<sup>2+</sup> implicates an ECCE mechanism for hydrogen production in aqueous solution.

